

1 **Title:** A pro-tumorigenic mDia2-MIRO1 axis controls mitochondrial positioning and function in
2 cancer-associated fibroblasts

3
4 **Authors:** Michael Cangkrama^{1*}, Huan Liu¹, James Whipman¹, Maria Zubair¹, Mai Matsushita¹,
5 Michela Di Filippo^{2,3}, Manfred Kopf¹, Metello Innocenti^{4*}, and Sabine Werner^{1*}

6
7 **Affiliations:**

8 ¹Institute of Molecular Health Sciences, Department of Biology, ETH Zurich, Otto-Stern-Weg 7,
9 8093 Zurich, Switzerland

10 ²Department of Dermatology, University Hospital of Zurich, 8091 Zurich, Switzerland

11 ³Faculty of Medicine, University of Zurich, 8091 Zurich, Switzerland

12 ⁴Heidelberg University Biochemistry Center, Heidelberg University, Heidelberg, Germany

13
14 ***Corresponding authors:**

15 Dr. Michael Cangkrama, Dr. Metello Innocenti and Prof. Dr. Sabine Werner

16 michael.cangkrama@biol.ethz.ch; metelloinnocenti@gmail.com; sabine.werner@biol.ethz.ch

17 Institute of Molecular Health Sciences, ETH Zürich, Hönggerberg, HPL F12, 8093 Zürich,
18 Switzerland. Phone: +41 44 633 3941, Fax: +41 44 633 1174

19
20 **Running Title:** mDia2–MIRO1 cross-talk promotes pro-tumorigenic protein secretion by CAFs

21 **Keywords:** Cancer-associated fibroblasts; mDia2; MIRO1; mitochondria; squamous
22 carcinogenesis

23 **Conflicts of interests**

24 The authors have declared that no conflict of interest exists.

25 **Abstract:** Cancer-associated fibroblasts (CAF) are key regulators of tumorigenesis. Further
26 insights into the tumor promoting mechanisms of action of CAFs could help improved cancer
27 diagnosis and treatment. Here we show that the formin mDia2 regulates the positioning and
28 function of mitochondria in dermal fibroblasts, thereby promoting a pro-tumorigenic CAF
29 phenotype. Mechanistically, mDia2 stabilized the mitochondrial trafficking protein MIRO1. Loss
30 of mDia2 or MIRO1 in fibroblasts or CAFs reduced the presence of mitochondria and ATP
31 levels near the plasma membrane and at CAF-tumor cell contact sites, caused metabolic
32 alterations characteristic of mitochondrial dysfunction, and suppressed the secretion of pro-
33 tumorigenic proteins. In mouse models of squamous carcinogenesis, genetic or pharmacological
34 inhibition of mDia2, MIRO1, or their common upstream regulator activin A inhibited tumor
35 formation. Consistently, co-upregulation of mDia2 and MIRO1 in the stroma of various human
36 cancers negatively correlated with survival. This work unveils a key role of mitochondria in the
37 pro-tumorigenic CAF phenotype and identifies an activin A/mDia2/MIRO1 signaling axis in
38 CAFs with diagnostic and therapeutic potential.

39
40 **Significance:** Inhibition of mDia2/MIRO1-mediated mitochondrial positioning in cancer-
41 associated fibroblasts induces mitochondrial dysfunction and suppresses tumor growth, revealing
42 a promising therapeutic strategy to target tumor-stroma crosstalk.

43 **Introduction**

44 Cancer-associated fibroblasts (CAFs) are major components of the tumor
45 microenvironment (TME), which, together with mutations and epigenetic alterations in the tumor
46 cells, plays a crucial role in determining malignancy. CAFs most often promote tumor growth
47 via paracrine control of cancer cells (1). This involves increased expression of cytokines, growth
48 factors and extracellular matrix (ECM) proteins and possibly alterations in protein secretion
49 pathways. Recent studies identified cytoskeletal abnormalities in CAFs (2), including
50 perturbations of the acto-myosin cytoskeleton, which impact on actin-based protrusions, cell
51 contractility and motility (3,4). A key regulator of the actin cytoskeleton is the formin mDia2
52 (DIAPH3) (5,6), which is upregulated in CAFs and promotes the CAF phenotype by enhancing
53 the formation of filopodia and cell migration, as well as the expression of CAF marker genes
54 (7,8). In dermal fibroblasts and skin CAFs, mDia2 is a downstream target of the pro-tumorigenic
55 cytokine activin A, a member of the transforming growth factor beta (TGF- β) superfamily that is
56 highly expressed by skin cancer cells and also by cells in the TME (9). Activin A induced the
57 expression of genes that encode pro-fibrotic and pro-tumorigenic proteins in dermal fibroblasts,
58 which in turn stimulate cancer cell proliferation and migration (7,10). The activin A-induced
59 increase in mDia2 levels prevent p53 nuclear accumulation, thereby promoting the expression of
60 CAF marker genes and pro-tumorigenic activities of fibroblasts (7). This paracrine axis is highly
61 relevant to human cancer as overexpression of both activin A and mDia2 correlates with poor
62 prognosis in several malignancies (7).

63 Here we discovered that mitochondrial positioning and function play a key role in
64 regulating the skin CAF phenotype and cancer progression, and depend on mDia2 and its ability
65 to stabilize the atypical Rho GTPase MIRO1 (RHOT1). Targeting the activin A-mDia2-MIRO1

66 signaling axis and the resulting mitochondrial/metabolic alterations in CAFs is therefore a
67 promising strategy for the treatment of different human cancers.

68 **Materials and Methods**

69 **Animals**

70 NOD/SCID (NOD.CB17-Prkdc^{scid}/NCrCrI) mice were housed under specific pathogen-free
71 conditions and received food and water *ad libitum*. Mouse maintenance and all animal
72 experiments were approved by the veterinary authorities of Zurich, Switzerland (Kantonales
73 Veterinäramt Zürich).

74

75 **Human skin cancer samples and CAFs**

76 Normal human skin and skin cancer samples were obtained anonymously from the Department
77 of Dermatology, University Hospital of Zurich (in the context of the Biobank project), approved
78 by the local and cantonal Research Ethics Committees. Normal skin was from healthy adult
79 volunteers or from the edges of skin tumors (SCCs), which had been diagnosed by experienced
80 pathologists. Written informed consent was obtained from all subjects, and the experiments
81 conformed to the principles set out in the WMA Declaration of Helsinki and the Department of
82 Health and Human Services Belmont Report.

83 CAFs were directly isolated from skin SCC biopsies alongside their paired normal skin
84 fibroblasts as described previously, with some modifications (11). Briefly, skin samples were
85 digested with trypsin, followed by digestion with collagenase. Cells were cultivated with J2
86 feeder cells. Fibroblasts/CAF were separated from SCC cells upon short incubation with trypsin
87 and then cultivated without feeder cells in DMEM, 10% fetal bovine serum (FBS), 1%
88 penicillin/streptomycin (P/S). The CAF phenotype was confirmed by expression of skin CAF
89 markers (12), and fibroblast cultures isolated from SCCs that did not have CAF properties were
90 excluded.

91 For fibroblast/CAF isolation from mouse ear tumors, we adapted a previously published protocol
92 (13). Briefly, the tumor was minced into small pieces and incubated with 2.5 ml of a collagenase
93 type II solution (500 U/ml; Worthington Biochemical Corporation, Lakewood, NJ) for 1 h at
94 37°C with manual agitation every 15 min. The cell suspension was poured through a 100 µm cell
95 strainer and the content centrifuged at 1,200 r.p.m. for 5 min. The resulting cell pellet was re-
96 suspended in 8 ml of DMEM/10% FBS/P/S and plated in two 6 cm dishes. Medium was changed
97 the following day, and cells were passaged prior to confluency.

98

99 **Cell lines**

100 HaCaT keratinocytes and SCC13 cells were obtained from Prof. Petra Boukamp, Leibniz
101 Institute Düsseldorf, Germany. Authentication of the cell lines was performed by the “Deutsche
102 Sammlung von Mikroorganismen und Zellkulturen” (DSMZ) GmbH, Braunschweig, Germany.
103 Absence of mycoplasma was confirmed by PCR using the PCR Mycoplasma Test Kit I/C
104 (PromoKine, Heidelberg, Germany) on a monthly basis.

105

106 **siRNA-mediated knock-down**

107 Knock-down of MIRO1 and mDia2 in primary human fibroblasts was performed using
108 previously characterized siRNAs (14-16). Cells were transfected with MIRO1, mDia2 or control
109 siRNAs using Lipofectamine™ RNAiMAX Transfection Reagent (Thermo Fisher Scientific,
110 Waltham, MA) according to the manufacturer's instructions and incubated for 24-48 h prior to
111 analysis. To visualize/confirm the knock-down efficiency *in vivo*, the siRNAs were pre-labeled
112 with fluorescein using the Label IT® siRNA Tracker™ (MIR 7216, MIRUS Bio LCC, Madison,
113 WI).

114

115 **Generation of human fibroblasts with shRNA-mediated knock-down of mDia2**

116 Primary human dermal fibroblasts (HDFs) were infected with lentiviruses pLKO.1-shmDia2
117 TRCN0000150903, which target mouse *mDia2* and human *DIAPH3*. The construct had been
118 previously characterized for specificity, and results had been confirmed with another shRNA
119 (17,18).

120

121 **Measurement of ATP and LDH levels**

122 ATP levels were measured using the CellTiter-Glo Assay according to the manufacturer's
123 instructions (Promega, Madison, WI). Briefly, cells were plated in triplicate in opaque 96-well
124 plates. After 24 h incubation, they were incubated for 10 min with CellTiter-Glo reagent, and
125 luminescence was measured using a 96-well plate reader. LDH assays were performed as
126 described previously (19).

127

128 **Analysis of cytokine concentrations**

129 The concentrations of several cytokines in the supernatant of fibroblasts were measured by
130 LEGENDplex human inflammation panel 1 (#740808, Biolegend) according to the
131 manufacturer's protocol. All samples were analyzed in technical duplicates, and averages of
132 biological replicates were used for statistical analysis. Flow cytometry was performed using a
133 BD LSRFortessa, and data were analyzed using FlowJo v10 (Tristar).

134

135 **Seahorse XF Cell Mito Stress Test**

136 Fibroblasts were plated in XF96 seahorse plates at 100,000 cells per well in DMEM/ 10% FCS/
137 PS), and the medium was subsequently switched to Seahorse XF base medium (103335-100,
138 Agilent Technologies, Santa Clara, CA) supplemented with 10 mM glucose or galactose, 1 mM
139 sodium pyruvate and 2 mM glutamine (assay concentration according to the manufacturer of the
140 kit:

141 [https://www.agilent.com/cs/library/usermanuals/public/XF_Cell_Mito_Stress_Test_Kit_User_G](https://www.agilent.com/cs/library/usermanuals/public/XF_Cell_Mito_Stress_Test_Kit_User_Guide.pdf)
142 [uide.pdf](https://www.agilent.com/cs/library/usermanuals/public/XF_Cell_Mito_Stress_Test_Kit_User_Guide.pdf)) and further incubated in a CO₂-free incubator for 1 h. Oligomycin, FCCP (carbonyl
143 cyanide-p-trifluoromethoxyphenylhydrazone) and antimycin A/rotenone were prepared in XF
144 assay medium with final concentrations of 1 μM, 1.5 μM and 1/0.1 μM, respectively, and
145 provided by the Seahorse XF Cell Mito Stress Test Kit (#103015-100; Agilent Technologies).
146 The compounds were serially injected to measure OCR of cells in the XF96 plate.

147

148 **Transfection of human fibroblasts**

149 Wild-type or mutant Flag-tagged mDia2 cDNAs (17,20) were subcloned into the retroviral pMX
150 vector (Cell Biolabs, San Diego, CA). pGEM-MIRO1 and cyto-Ruby3-iATPSnFR^{1.0} (ATP
151 biosensors (21)) plasmids were purchased from Sino Biological Inc. (Beijing, China, #HG15898-
152 G) or Addgene (Watertown, MA, #102551), respectively. Plasmid vectors and Lipofectamine™
153 2000 (#11668030, Invitrogen, Carlsbad, CA) were incubated with Opti-MEM™ I Reduced
154 Serum Medium (#31985062, Thermo Fisher Scientific) at room temperature for 20 min. The
155 mixture was then added to primary human fibroblasts. After 6 h incubation, the medium was
156 replaced by normal culture medium containing 10% FBS. Cells were allowed to recover for 24-
157 48 h prior to analysis.

158

159 **ER and mitochondrial staining**

160 Fibroblasts were seeded on glass coverslips in 24-well plates with complete medium and
161 incubated at 37° C. They were stained with ER-Tracker™ Blue-White DPX (Thermo Fisher
162 Scientific, E12353), MitoTracker-Green (Thermo Fisher Scientific, M7514), CellROX-Orange
163 (Thermo Fisher Scientific, C10443), MitoSOX-Red (Thermo Fisher Scientific, M36008) or
164 MitoTracker Red CMXRos (Thermo Fisher Scientific, M7512) diluted 1:1000 in complete
165 medium for 45 min at 37° C. Subsequently, cells were washed and fixed with 3.7%
166 formaldehyde in complete medium for 15 min at 37° C. After washing, they were mounted with
167 Mowiol (Sigma-Aldrich, St. Louis, MO). Images were acquired with an Axio Imager.A1
168 microscope (Carl Zeiss AG, Oberkochen, Germany).

169

170 **RNA isolation and qRT-PCR**

171 RNA isolation and quantitative qRT-PCR were performed as described (13) using the primers
172 listed in Supplementary Table 1. Values obtained for the first control were set to 1.

173

174 **Histology, immunostaining, and image analysis**

175 Histological analysis and immunostainings were performed as described (13) using the
176 antibodies listed in Supplementary Table 2. Immunofluorescence images were analyzed in Fiji
177 (22) and normalized to cell number for *in vitro* experiments with at least 9 microscopic fields of
178 view for each condition analyzed. Curvature of ECM fibers *in vivo* was analyzed with the ImageJ
179 quantification tool TWOMBLI (23). Mitochondrial networks were analyzed using MiNA (24).
180 Mitochondrial and ATP distribution were determined by measurement of MitoTracker or ATP
181 biosensor fluorescence intensity relative to the highest intensity value. We calculated the average

182 for every 10% incremental distance from the perinuclear region to the plasma membrane using
183 ImageJ (Fiji) plot-profile tool. The relative distance is indicated with values from 1 - 10; at least
184 100-200 intensity profiles were measured. All images were processed in an identical way by
185 adjusting brightfield/contrast and subtracting background signal to identify cell edge/contour
186 using a wide-field microscope.

187

188 **Proximity ligation assay**

189 Proximity ligation assays (PLA) were performed with mDia2 (sc-293288, Santa Cruz, Santa
190 Cruz, CA), MIRO1 (NBP1-59021, Novus Biologicals, Littleton, CA) and TRAK1 (H00022906-
191 M01A, Thermo Fisher Scientific) antibodies (1:500) and MitoTracker Green as described for
192 fluorescence microscopy, followed by ligation of probes specific for each antibody using a PLA
193 Kit (DUO92101, Sigma-Aldrich). Samples treated without primary antibodies were used as
194 negative controls.

195

196 **Preparation of protein lysates and Western blot analysis**

197 Preparation of protein lysates and Western blot were performed as previously described (13).
198 Some lysates were collected from cells pre-treated with the proteasome inhibitor epoxomicin (10
199 μ M) (S2619, Selleckchem, Houston, TX), the mDia2 inhibitor SMIFH2 (25 μ M) (S4826, Sigma-
200 Aldrich) or recombinant activin A (20 ng/ml) (#120-14, PeproTech, Cranbury, NJ).
201 Antibodies against INHBA (sc166503, Santa Cruz, Santa Cruz, CA, 1:500 diluted), mDia2
202 (recognizing both the murine and human proteins; 1:5,000 diluted) (17,18), α -SMA (A2547,
203 Sigma-Aldrich, 1:500 diluted), HSP60 (ab59457, Abcam, Cambridge, UK, 1:500 diluted), FN1
204 (ab2413, Abcam, 1:500 diluted), COL4A1 (#10710, Progen, Heidelberg, Germany, 1:500

205 diluted), ELN (ab21610, Abcam, 1:500 diluted), MIRO1 (NBP1-59021, Novus Biologicals,
206 Littleton, CA, 1:500 diluted), POSTN (ab14041, Abcam, 1:500 diluted), calnexin (NB300-518,
207 Novus Biologicals, 1:500 diluted), GM130 (MABT1363, Sigma-Aldrich, 1:500 diluted),
208 GAPDH (5G4, HyTest, Turku, Finland, 1:10,000 diluted), α -tubulin (T5168, Sigma-Aldrich,
209 1:10,000 diluted), and vinculin (V4505, Sigma-Aldrich, 1:2,000 diluted), were used. Secondary
210 antibodies were anti-rabbit or anti-mouse IgG (W4011 and W4021, Promega, 1:8,000 diluted)
211 conjugated with horseradish peroxidase, and chemiluminescence was determined using the
212 WesternBright ECL Detection System (Advansta, San Jose, CA). Bands were visualized using
213 Fusion Solo 6S (Witec AG, Sursee, Switzerland), and intensity was quantified with ImageJ
214 software (National Institutes of Health, Bethesda, MD). Loading controls of different molecular
215 weight were used depending on the protein that was analyzed in the experiment.

216

217 **Chromatin immunoprecipitation (ChIP)**

218 HDFs (approx. 5×10^8 cells) at 80–90% confluency, which had been pre-treated with activin A
219 (20 ng/ml) for 6 h, were collected, resuspended in DMEM, and subjected to ChIP as previously
220 described (25). The purified DNA fragments were used for PCR amplification using the primers
221 listed in Supplementary Table 3.

222

223 **Migration assays**

224 For scratch assays, cells were grown to 100% confluency and treated with 2 μ g/ml mitomycin C
225 (Sigma-Aldrich) for 2 h to inhibit cell proliferation. One or several scratches were made into the
226 cell layer using a sterile 200 μ l pipette tip. Dead cells and debris were washed off with pre-

227 warmed PBS. The same area was photographed directly after scratching and at different time
228 points thereafter.

229 To determine the capacity of the matrix deposited by fibroblasts to stimulate SCC cell migration,
230 SCC13 cells were seeded on culture inserts (#80209, Ibidi, Gräfelfing, Germany) that were
231 placed on top of the matrix that had been deposited by fibroblasts. The insert was then removed
232 for migration assays.

233 Chemotactic transwell migration was assessed as described (7). Briefly, SCC13 cells were
234 seeded on the insert of the transwell plates in DMEM/1% FBS and let to migrate for 24 h
235 towards CM from fibroblasts.

236

237 **Isolation of fibroblast secretomes and matrisomes**

238 Cells were plated at 70-90% confluency in DMEM/10% FBS/P/S. On the following day, they
239 were pre-treated with 2 µg/ml mitomycin C and cultured in starvation medium (DMEM/1 %
240 FBS/P/S) with 1 µg/ml doxycycline (DOX) for an additional 3 days. Conditioned media and
241 ECM were prepared as previously described (13). Total secreted protein concentration was
242 determined using the Bradford method (26).

243

244 **Skin tumorigenesis assays**

245 Tumorigenesis assays in mouse ear skin were performed as described (12). Briefly, 3 µl cell
246 suspension (2×10^5 cancer cells in Hanks` s buffer) was injected intradermally into the ear of
247 NOD/SCID mice. For tumor cell/fibroblast co-injection experiments, we injected 10^5 cancer
248 cells and an equal number of fibroblasts. Tumor formation was monitored over 2-5 weeks,
249 followed by sacrifice of the animals and analysis of the isolated tumors.

250 For MIRO1-Reducer treatment experiments, SCC13 cells and primary human CAFs were co-
251 injected intradermally, and tumor formation was observed during 2 weeks. Tumors were then
252 treated with MIRO1-Reducer (2.5 μ M) (#7091, Tocris, Bristol, UK) or vehicle (DMSO) every 3–
253 4 days by direct injection into the tumor. Tumors were harvested three days after the last
254 injection.

255

256 **Spheroid formation and growth assay**

257 Spheroid assays were performed and reported according to experimental parameters proposed by
258 The MISpheroID Consortium (27). Twenty μ l conditioned media from primary human skin
259 fibroblasts (pre-conditioned medium: DMEM/1% FBS/1% P/S) and containing 2,000 SCC13
260 cells were placed on the lids of 6 cm culture plates using a hanging-drop method (28). To prevent
261 dehydration, 5 ml PBS were added to the bottom. Cells were incubated at 37°C and 5% CO₂.
262 Spheroids were incubated for 3 days and analyzed for increase in spheroid area.

263

264 **Bioinformatic analysis**

265 Gene expression data for *MIRO1* were acquired from publicly available gene expression
266 profiling data of human cancers (GSE45001, GSE9014, and GSE40595) and analyzed using the
267 GEO2R analysis tool in the GEO database (29) and Gene Expression Profiling Interactive
268 Analysis 2.0 (GEPIA2) (30). Single cell RNA sequencing (scRNA-seq) data from melanomas
269 were investigated through the use of publicly available scRNA datasets
270 (https://singlecell.broadinstitute.org/single_cell). The correlation between *MIRO1* expression and
271 expression of other genes in pan-cancer was investigated using Tumor IMMune Estimation
272 Resource 2 (TIMER2) (<http://timer.cistrome.org/>) (31). The effect of MIRO1 knock-down in

273 genome-wide knock-down screens was analyzed using DepMap (DepMap.org). Survival graphs
274 were generated based on the PROGene gene expression–based survival analysis web
275 application by using median gene expression value as a dividing point, and statistical analysis of
276 patient survival data was done as described (32).

277

278 ***Ex vivo* tumor explant cultures**

279 Ear skin tumors were cut into fragments of approximately 0.5 cm² and cultured at the air–liquid
280 interface in DMEM/10% FBS supplemented with 5 µg/ml insulin (I5500), 0.1 nM cholera toxin
281 (C8052), 10 ng/ml epidermal growth factor (E4127), 50 IU/ml P/S and 0.4 µg/ml hydrocortisone
282 (#386698) (all from Sigma-Aldrich). After overnight incubation, they were treated with
283 follistatin (50 ng/ml) (#120-13, Peprotech, Rocky Hill, NJ) for 6 h and embedded in paraffin.

284

285 **Mitochondrial extraction**

286 Mitochondrial extraction was carried out using the Mitochondria Isolation Kit for Cultured Cells
287 (#89874, Thermo Fisher Scientific). In brief, 20,000,000 primary human fibroblasts were
288 trypsinized, suspended in 1 ml of complete DMEM and centrifuged at 850 g for 2 min. The
289 supernatant was discarded, and 800 µl Reagent A (with 1x cComplete™ EDTA-free cocktail
290 proteinase inhibitor (Sigma-Aldrich)) was added to the pellet. After vortexing at medium speed
291 for 5 sec, the samples were incubated on ice for 2 min. Ten µl of Reagent B were then added and
292 vortexed for 5 sec. The cells were then incubated on ice for 5 min, vortexing every minute. 800
293 µl of Reagent C (with 1x cComplete™ EDTA-free cocktail proteinase inhibitor) were then added
294 and the cells were inverted several times. Samples were centrifuged at 700 g for 10 min at 4° C.
295 The pellet contained the total cell lysate and was stored at -20°C. The supernatant was collected

296 and centrifuged again at 3,000 g for 15 min. The resultant supernatant (cytosolic fraction) and
297 the pellet (mitochondrial fraction) were stored at -20°C.

298

299 **Statistical analysis**

300 Statistical analysis was performed using the PRISM software, version 9 for Mac OS X or
301 Windows (GraphPad Software Inc, San Diego, CA). For comparison of two groups, unpaired
302 Student's t-test was performed; for comparison of more than two groups, one-way or two-way
303 ANOVA and Bonferroni's multiple comparisons test were used. Non-significant (ns) $p > 0.05$,
304 $*p < 0.05$, $**p < 0.01$, $***p < 0.001$, $****p < 0.0001$.

305

306 **Data availability**

307 The data generated in this study are available within the article and its Supplementary Data files.

308

309

310 **Results**

311 *mDia2 promotes protein secretion and ECM deposition by primary human fibroblasts*

312 The key role of mDia2 in fibroblast-CAF reprogramming (7,8) and the pivotal
313 contribution of CAF-derived soluble factors and ECM proteins to cancer progression (33),
314 prompted us to assess the involvement of mDia2 in the production of a pro-tumorigenic
315 matrisome and secretome. Knock-down of mDia2 in primary human dermal fibroblasts (HDF)
316 using shRNA (sh-mDia2) (17) indeed reduced the overall amounts of secreted proteins compared
317 to cells transduced with lentiviruses carrying an empty vector (sh-EV cells) (**Fig. 1A**). The levels
318 of secreted fibronectin 1 (FN1) and collagen IV (COL4), and of activin A (9) (encoded by the
319 *INHBA* gene), which follow the classical ER-Golgi secretion pathway (34), were markedly
320 reduced by mDia2 knock-down, while their intracellular levels were not affected (**Fig. 1B-E**).
321 This suggested that mDia2 regulates protein secretion. Indeed, the ECM deposited by the sh-
322 mDia2 cells was strongly depleted of FN1, COL1 and elastin (ELN), and the conditioned
323 medium (CM) of sh-mDia2 cells contained significantly lower amounts of IFN- α 2, IL-1 β , and
324 IL-6, compared to control cells (**Fig. 1F, G**). Importantly, it failed to promote anchorage-
325 independent spheroid growth of SCC13 cells (**Fig. 1H**). mDia2 knock-down HDFs also showed
326 less stress fibers, and reduced migratory abilities (**Fig. 1I-K**). These phenotypes, as well as the
327 reduced FN1 secretion, were rescued by re-expression of wild-type mDia2, but not of an actin
328 polymerization-deficient mDia2 mutant (17,35) (**Fig. 1J-L**). Neither wild-type nor mutant
329 mDia2 expression affected the intracellular FN1 levels (**Fig. 1M**).

330

331 *mDia2 regulates mitochondrial distribution and function in fibroblasts*

332 To unravel how mDia2 regulates protein secretion, we analyzed key components of the
333 secretory pathway. mDia2 knock-down HDFs showed the expected size increase (7,35), but they

334 neither exhibited obvious morphological abnormalities of the endoplasmic reticulum (ER), the
335 Golgi apparatus, or the microtubule network nor significant differences in the levels of the ER or
336 Golgi markers calnexin and GM130, respectively (Supplementary Fig. S1A-D).

337 Given that efficient protein secretion requires a high cellular metabolic activity and intact
338 mitochondria (36), and that the actin cytoskeleton contributes to the structural integrity and
339 dynamics of mitochondria (37), we stained mitochondria in mDia2 knock-down HDFs with
340 MitoTracker. mDia2 depleted cells showed perinuclear clustering of mitochondria, whereas
341 mitochondria in control fibroblasts were evenly distributed from perinuclear to peripheral
342 regions (**Fig. 2A**). These results were verified with two published siRNAs (16) and with HDFs
343 from two different donors (Supplementary Fig. S1E-I). There was also a small increase in
344 mitochondrial mean branch length and network branch in sh-mDia2 fibroblasts, indicative of
345 elongated and hyper-fused mitochondria. Furthermore, the localization of mDia2 in primary
346 human foreskin and breast skin fibroblasts was suggestive of an association with the
347 mitochondrial network (Supplementary Fig. S2A, B). Co-staining with MitoTracker supported
348 this association in human fibroblasts, whereas the co-localization of mDia2 and mitochondria
349 was less obvious in different epithelial cell lines (Supplementary Fig. S2C). Western blot
350 analysis of subcellular fractions of HDFs confirmed the known localization of mDia2 in the
351 cytoplasm of fibroblasts (7), but also showed its association with mitochondria. The
352 mitochondria-binding protein MIRO1 and the mitochondrial matrix and housekeeping protein
353 HSP60 served as positive controls (**Fig. 2B**). The partial co-localization of MIRO1 and mDia2 in
354 skin fibroblasts bolsters this conclusion (Supplementary Fig. S2D). Proper mitochondrial
355 distribution in mDia2 knock-down fibroblasts was restored upon re-expression of wild-type

356 mDia2, but not of the IA mutant (**Fig. 2C, D**). Moreover, wild-type mDia2 partially rescued
357 mitochondrial topology (Supplementary Fig. S2E).

358 The altered position and topology of mitochondria in the mDia2 knock-down fibroblasts
359 were accompanied by a strong increase in intracellular reactive oxygen species (ROS) and
360 mitochondrial superoxide levels (**Fig. 2E, F**). However, this did not affect cell viability as shown
361 by measurement of lactate dehydrogenase (LDH) in the supernatant (**Fig. 2G**). Total intracellular
362 ATP levels were only mildly affected (**Fig. 2H**). Re-expression of wild-type mDia2, but not of
363 the IA mutant, rescued and even further increased intracellular ATP levels compared to control
364 cells (**Fig. 2H**). Levels of mitochondrial DNA and of HSP60 were only slightly reduced in the
365 mDia2 knock-down cells (**Fig. 2I, J**), suggesting that the increased ROS levels are not a
366 consequence of an increase in the number of mitochondria.

367 Replacing glucose in the cell culture medium by galactose allows unmasking
368 mitochondrial dysfunctions, particularly defects in oxidative phosphorylation (OXPHOS),
369 because (i) cells rely on OXPHOS for efficient ATP production and (ii) oxidation of galactose to
370 pyruvate via glycolysis does not yield net ATP (38). When cultured in the presence of galactose,
371 the mDia2 knock-down fibroblasts displayed an even more dramatic reduction in the secretion of
372 FN1 and COL1 (**Fig. 2K vs. 1F**). This correlated with impairments in the mitochondrial oxygen
373 respiration rate (OCR) and reduced ATP-linked mitochondrial respiration in mDia2 knock-down
374 vs. control fibroblasts (**Fig. 2L**). Only a slight reduction in the basal respiration rate was
375 observed in medium with glucose, suggesting partial compensation by glycolysis
376 (Supplementary Fig. S2F). The basal OCR/ECAR (extracellular acidification rate) ratio of
377 mDia2 knock-down fibroblasts was significantly higher compared to control cells, indicating

378 their relatively higher reliance on mitochondrial OXPHOS (Supplementary Fig. S2G). These
379 results identify mitochondrial dysfunction in mDia2 knock-down fibroblasts.

380

381 *mDia2 stabilizes the mitochondrial trafficking protein MIRO1*

382 Our results raise the possibility that mDia2 affects proteins involved in mitochondrial
383 trafficking. Among them, Rho-GTPase MIRO1/RHOT1 (39) was an attractive candidate. Indeed,
384 MIRO1 protein, but not mRNA levels were strongly reduced in the mDia2 knock-down
385 fibroblasts (**Fig. 3A, B**). Knock-down of mDia2 in fibroblasts also reduced MIRO1 protein levels
386 in the mitochondrial fraction (**Fig. 3C**). MIRO1 co-localized with mitochondria and clustered in
387 the perinuclear region of sh-mDia2 fibroblasts (**Fig. 3D**).

388 Re-expression of wild-type, but not IA mDia2, partially restored MIRO1 protein levels in
389 the mDia2 knock-down fibroblasts (**Fig. 3E**). Consistent with the findings that mDia2 increases
390 proteasome activity (20) and that ubiquitinated MIRO1 is targeted for proteasomal degradation
391 (40), the proteasome inhibitor epoxomicin partially rescued MIRO1 protein levels in the mDia2
392 knock-down fibroblasts and normalized their mitochondrial distribution and topology (**Fig. 3F,**
393 **G**). The stabilization of MIRO1 by mDia2 is likely the consequence of their physical interaction
394 as supported by PLA (**Fig. 3H**). PLA combined with MitoTracker staining showed that the
395 mDia2-MIRO1 complex localizes to mitochondria (**Fig. 3I**).

396

397 *mDia2 and MIRO1 levels in human cancer stroma are predictors of poor prognosis*

398 We next tested if MIRO1 is abnormally expressed and functionally relevant in human
399 cancer tissue. We first made use of the Cancer Dependency Map (Depmap), a genome-wide loss-
400 of-function screening database (41), to determine the effect of MIRO1 knock-down on cancer

401 features. Dependency score analysis showed that MIRO1 plays an integral role in the
402 proliferation and survival of various cancer cells (Supplementary Fig. S3A). Analysis of data
403 from “The Cancer Genome Atlas” (TCGA) revealed a consistent upregulation of *MIRO1* in the
404 stroma of liver, breast and ovarian cancer in comparison to stroma of healthy tissue (**Fig. 4A**),
405 which was not observed in bulk tumor tissue (Supplementary Fig. S3B). ScRNA-seq showed
406 remarkable co-expression of *DIAPH3* and *MIRO1* in melanoma CAFs (**Fig. 4B**). Strong
407 expression of *MIRO1* positively correlates with that of *mDia2* and *INHBA*, but not of *TGFBI*, in
408 different cancers (**Fig. 4C**). Kaplan–Meier survival analysis showed a strong association of high
409 co-expression of *mDia2* and *MIRO1* with decreased survival of patients with liver or lung cancer
410 (**Fig. 4D**). Notably, numbers of MIRO1-positive cells were much higher in the stroma of
411 epithelial skin cancers than in healthy skin (**Fig. 4E**). Co-staining of SCC sections for MIRO1
412 and the pan-fibroblast marker PDGFR- α indicated that many of the MIRO1-positive cells are
413 indeed fibroblasts. Co-expression of both proteins was less pronounced in normal skin
414 (Supplementary Fig. S3C). These findings point to a pro-tumorigenic effect of MIRO1 in CAFs
415 of different human cancers, although an additional pro-tumorigenic function of this protein in
416 cancer cells or other cells of the TME cannot be excluded.

417 To assess the functional relevance of the high MIRO1 levels in CAFs for cutaneous SCC
418 pathogenesis, we used low-passage primary CAFs and matched normal HDFs (NF) from human
419 SCC lesions and non-tumorigenic skin, respectively. The cultured CAFs showed a significantly
420 higher expression of MIRO1, *mDia2* and other CAF markers, such as *INHBA* and *FN1*,
421 compared to NFs, and they strongly promoted anchorage-independent growth of SCC13 cells in
422 spheroids (**Fig. 4F-H**). The increased expression of *mDia2* and MIRO1 in CAFs vs. NFs did not
423 further enhance peripheral mitochondrial positioning (**Fig. 4I**). However, using a fluorescent

424 ATP sensor, we found that ATP was clearly detectable at the cell periphery of CAFs, but not of
425 NFs from two different donors, while strong perinuclear fluorescence was observed in both
426 CAFs and NFs (**Fig. 4J**, Supplementary Fig. S3D). Thus, ATP levels near the plasma membrane,
427 which are required to supply energy for protein secretion (42), are higher in CAFs compared to
428 NFs. Mitochondria were also more fragmented in CAFs, resulting in decreased median branch
429 length (**Fig. 4K**). MIRO1, in complex with TRAK1 and microtubule motor proteins, regulates
430 anterograde mitochondrial movement in mammalian cells, the increase of which promotes cancer
431 cell invasiveness and viability (43). Using PLA, we found a higher MIRO1-TRAK1 interaction
432 in CAFs vs. NFs (Supplementary Fig. S3E). These findings strongly suggest that mitochondrial
433 trafficking and function are altered in CAFs, thereby promoting protein secretion. Indeed,
434 deposition of FN1 and COL1 was strongly increased in the same CAFs (**Fig. 4L**).

435 Overexpression of MIRO1 in NFs recapitulated the pro-tumorigenic secretion-dependent effects
436 of CAFs. In particular, isolated CM and decellularized ECM from NFs overexpressing MIRO1
437 promoted spheroid formation and proliferation of the weakly malignant SCC13 cell line (**Fig.**
438 **4M, N**). This is in line with their increased deposition of the pro-tumorigenic ECM proteins FN1
439 and COL1 (**Fig. 4O**). Treatment of MIRO1-overexpressing fibroblasts with FCCP to disrupt the
440 mitochondrial membrane potential and consequent ATP production reduced the deposition of
441 FN1 and COL1 (Supplementary Fig. 3F, G). This further supports the functional link between
442 mitochondrial activity and the secretion of pro-tumorigenic proteins by fibroblasts with high
443 MIRO1 levels. Finally, overexpression of wild-type MIRO1 in mDia2 knock-down fibroblasts
444 rescued their mitochondrial distribution defect (**Fig. 4P, Q**).

445

446 *MIRO1 is a target of activin A/Smad2/3 signaling in fibroblasts*

447 The co-upregulation of *INHBA*, *mDia2* and *MIRO1* in CAFs raised the question as to
448 whether *MIRO1* expression is also controlled by activin A. Indeed, treatment of HDFs with
449 activin A increased the expression of *MIRO1* (**Fig. 5A**). We identified a conserved SMAD
450 binding element (SBE) within the 2-kb region upstream of the *MIRO1* gene transcription start
451 site (TSS), and activin A promoted binding of SMAD2/3 to this SBE (**Fig. 5B**). *In vivo*, *MIRO1*
452 was strongly expressed in the stroma of xenograft tumors that formed upon injection of SCC13
453 cells overexpressing *INHBA* (7) into the ear skin of immuno-deficient NOD/SCID mice (**Fig.**
454 **5C**). *Vice versa*, overexpression of the secreted activin antagonist follistatin in SCC13 cells (7)
455 reduced the expression of *MIRO1* in the stroma, and a similar effect was observed when biopsies
456 from tumors generated by wild-type SCC13 cells were treated *ex vivo* with follistatin (**Fig. 5D,**
457 **E**). Characterization of HDFs with DOX-inducible expression of follistatin (Fb FST) showed that
458 both the mRNA and protein levels of *MIRO1* and *mDia2* were significantly down-regulated
459 (**Fig. 5F-I**). Furthermore, Fb FST exhibited changes in mitochondrial distribution (**Fig. 5J**),
460 resembling those observed in *mDia2*-depleted fibroblasts. These abnormalities as well as the
461 reduced efficacy of CM of Fb FST to promote anchorage-independent growth of SCC13 cells in
462 spheroids were rescued by overexpression of *MIRO1* in these cells (**Fig. 5K-M**). These results
463 demonstrate that *MIRO1* is a direct and functionally relevant target of activin A.

464

465 *MIRO1* is required for efficient protein secretion by CAFs

466 Given the crucial role of *mDia2* in the conversion of murine dermal fibroblasts into pro-
467 tumorigenic CAFs (7), we determined if knock-down of *MIRO1* had a similar effect as knock-
468 down of *mDia2*. *MIRO1* silencing in patient-derived CAFs (**Fig. 6A, B** and Supplementary Fig.
469 S4A) had no effect on the expression of major skin CAF marker genes. Accordingly, nuclear p53

470 levels in si-MIRO1 cells were similar to those in control cells (**Fig. 6C**). In addition, MIRO1
471 silencing did not affect the expression of other small GTPases (*RHOA*, *CDC42*, *RALA* and
472 *RHOT2*) (12,44) (**Fig. 6D**). However, it caused the expected perinuclear mitochondrial
473 clustering, reduced the deposition of COL1 and also enhanced the levels of mitochondrial
474 superoxide (**Fig. 6E-G**). When we cultured si-MIRO1 cells in medium containing high glucose,
475 total cellular ATP levels were not reduced by MIRO1 knock-down (Supplementary Fig. S4B), as
476 previously shown with other cells (45,46). However, the distribution of intracellular ATP was
477 affected, with ATP being reduced at the cell periphery (Supplementary Fig. S4C). When cells
478 were cultured in medium containing galactose instead of glucose, MIRO1 knock-down caused a
479 significant reduction of total cellular ATP levels and an even more dramatic increase in
480 mitochondrial superoxide (Supplementary Fig. S4D, E vs. **Fig. 6G**). This correlated with lower
481 proliferation and migration rates of si-MIRO1 CAFs in medium with galactose (Supplementary
482 Fig. S4F, G). Survival of MIRO1 knock-down cells was reduced in medium with galactose, but
483 not in medium with glucose (**Fig. 6H**). Basal and maximal OCR as well as ATP-linked OCR
484 were significantly lower in si-MIRO1 vs. control CAFs cultured in the presence of galactose, but
485 not in the presence of glucose (**Fig. 6I**). These results suggest that MIRO1 knock-down cells fail
486 to increase their oxygen consumption capacity via OXPHOS when cultured in galactose medium
487 and further points to their mitochondrial dysfunction.

488 Overall protein secretion was already reduced in the MIRO1 knock-down CAFs when
489 cultured in glucose medium, and they deposited much less FN1 and COL1 (**Fig. 6J-L**).
490 However, expression of the CAF markers *INHBA* and *ACTA2* was comparable at the RNA (**Fig.**
491 **6D**) and protein levels (**Fig. 6M**). Similar results were obtained using a second siRNA
492 (Supplementary Fig. S4H, I). HDFs with DOX-inducible overexpression of *INHBA* (Fb Act),

493 which acquire a CAF phenotype (7), confirmed these findings. In these cells, the knock-down of
494 MIRO1 significantly reduced the secretion of mature activin A and resulted in the concomitant
495 intracellular accumulation of the INHBA precursor, while INHBA mRNA levels were not
496 affected (Supplementary Fig. S5A-E). Taken together, we observed similar changes in protein
497 secretion and mitochondrial positioning in fibroblasts with either MIRO1 or mDia2 knock-down.

498

499 *mDia2 and MIRO1 position mitochondria at CAF-tumor cell contact sites to support the pro-*
500 *tumorigenic activity of CAFs*

501 We next analyzed co-cultures of SCC13 cells with either sh-EV or sh-mDia2 fibroblasts
502 and found that mitochondria in control fibroblasts were much closer to SCC13 cells (**Fig. 7A, B**).
503 Pharmacological inhibition of formins in SCC patient-derived CAFs by 25 μ M SMIFH2, a dose
504 that is optimal for mDia2 inhibition (18), reduced the levels of mDia2 and also those of MIRO1
505 (**Fig. 7C**). This correlated with a reduction in F-actin staining and perinuclear mitochondrial
506 clustering in SMIFH2-treated CAFs (**Fig. 7D**). Importantly, SMIFH2-treated HDFs displayed
507 reduced secretion of FN1 and COL1, but no significant changes in their intracellular levels
508 (Supplementary Fig. S6A, B). These data support the relevance of mDia2-dependent regulation
509 of MIRO1 and mitochondria in NFs and patient-derived CAFs, which may affect cancer cells by
510 regulating protein secretion.

511 To test the relevance of MIRO1 in CAFs for squamous carcinogenesis, we co-cultured
512 SCC13 cells with si-MIRO1 CAFs. These cells exhibited a similar defective mitochondrial
513 distribution as sh-mDia2 fibroblasts (**Fig. 7E**). Consistently, incubation of SCC13 cells with CM
514 collected from si-MIRO1 or control patient CAFs showed that the CM from the si-MIRO1 CAFs
515 was significantly less efficient in promoting migration and anchorage-independent growth of the

516 tumor cells in chemotactic transwell and spheroid formation assays (**Fig. 7F, G**). When we
517 plated SCC13 cells on the de-cellularized matrix deposited by either control or si-MIRO1 CAFs,
518 the colony-forming and migratory capacities of the cancer cells were significantly lower on
519 matrix deposited by si-MIRO1 CAFs (Supplementary Fig. S7A, B).

520 *In vivo*, intradermal co-injection of SCC13 cells (**Fig. 7H**) or of highly malignant A431
521 carcinoma cells (Supplementary Fig. S7C) and control primary human SCC CAFs into the ear of
522 NOD/SCID mice resulted in rapid and efficient tumor formation. These data clearly demonstrate
523 a pro-tumorigenic effect of MIRO1 in human fibroblasts. The tumors showed invasive growth,
524 which was much less pronounced when si-MIRO CAFs were used (**Fig. 7H**, inset). Reduced
525 expression of MIRO1 in the stroma of the few palpable tumors that developed under these
526 conditions and in fibroblasts isolated from resected tumors was still visible at the assay end point
527 (Supplementary Fig. S7D-G). This correlated with significantly reduced deposition of collagen
528 and increased collagen curvature (**Fig. 7I-J**), a feature of non-malignant matrix remodeling (47).
529 Tumor cell proliferation was also reduced, while there was no difference in the area covered by
530 blood or lymphatic vessels (Supplementary Fig. S7H, I). Finally, we assessed the therapeutic
531 potential of MIRO1 inhibition *in vivo*. Palpable ear skin xenograft tumors formed by SCC13
532 cells and primary human CAFs were injected with "MIRO1-Reducer" (48) every 3-4 days over
533 18 days to induce degradation of MIRO1. Remarkably, this treatment strongly suppressed tumor
534 growth (**Fig. 7K**) and correlated with reduced MIRO1 protein levels in the fibroblasts isolated
535 from the treated tumors (Supplementary Fig. S7J).

536 Taken together, these results demonstrate that MIRO1 is required for the efficient
537 secretion of proteins from CAFs, which promotes cancer-cell proliferation and malignant SCC
538 growth. Furthermore, they show that mDia2 acts through MIRO1 and mitochondria to control

539 pro-tumorigenic protein secretion and matrix deposition *in vivo*. Finally, they identify mDia2 and
540 MIRO1 as important stromal targets for cancer therapy.

541 **Discussion**

542 We discovered a key role of mDia2 in the regulation of protein secretion by HDFs and
543 CAFs, which involves stabilization of MIRO1 as well as appropriate positioning of mitochondria
544 and ATP production at the cell periphery. While recent studies have highlighted the importance
545 of cellular metabolism for matrix protein synthesis in fibroblasts (49) and of metabolic
546 reprogramming in the acquisition of a CAF phenotype (50), our work reveals that proper
547 mitochondrial distribution and activity strongly impact on the secretion of pro-tumorigenic
548 proteins by these cells. Knock-down of mDia2 impaired this process and led to intracellular
549 accumulation of otherwise secreted proteins. Our biochemical and microscopy data demonstrate
550 that mDia2 is associated with mitochondria in skin fibroblasts. These findings are consistent with
551 actin assembly being implicated in reorganizing and shuffling mitochondria during mitosis and
552 mitophagy (37,51). Some of the molecular players involved in these actin-based processes are
553 known (52), but neither mDia2's association with mitochondria nor its role in the regulation of
554 mitochondrial distribution and function had been described. Furthermore, we discovered that
555 mDia2 interacts with MIRO1 and that MIRO1 is essential to sustain the pro-tumorigenic
556 activities of skin CAFs by allowing appropriate mitochondrial distribution and metabolic
557 functions. First, we show that not only mDia2, but also MIRO1 is overexpressed in the stroma of
558 various cancers, and that their combined overexpression correlates with reduced survival of
559 patients with liver, lung, or pancreatic cancer. Second, knock-down of either mDia2 or MIRO1
560 strongly reduced the pro-tumorigenic effects of patient-derived skin cancer CAFs *in vitro* and *in*
561 *vivo*. The reduction in mDia2 and/or MIRO1 expression was associated with inefficient
562 OXPHOS, reduced ATP levels – in particular at the cell periphery-, and significantly reduced
563 deposition of matrix proteins by CAFs. This is not the result of a transcriptional effect, since

564 MIRO1 silencing did not alter the expression of several CAF marker genes. Rather, impaired
565 mitochondrial distribution and function in these cells provide a likely explanation for the
566 observed secretory deficiency. This is consistent with the important role of MIRO1 in the release
567 of neurotransmitters and insulin from presynaptic nerve terminals or pancreatic β -cells,
568 respectively (53,54), and the positioning of mitochondria near secretory sites, thereby supplying
569 ATP to support exocytosis (55). The co-expression of mDia2 and MIRO1 is at least in part
570 controlled by activin A-Smad2/3 signaling. Two independent mechanisms allow mDia2 to
571 regulate MIRO1 expression: the first mechanism involves a positive feedback loop whereby high
572 mDia2 levels promote *INHBA*/activin A expression in fibroblasts and its secretion, which in turn
573 increases *mDia2* and *MIRO1* transcription in these cells ((7) and this study). The second relies on
574 the ability of mDia2 to stabilize MIRO1 in fibroblasts, possibly by preventing its proteasomal
575 degradation (this study). The mDia2-MIRO1 interaction may contribute to this effect, since
576 mDia2 binds to ubiquitinated proteins and reduces proteasomal activity (20).

577 Given that optimal MIRO1 expression is key to the maintenance of a pro-tumorigenic
578 CAF phenotype, follistatin, neutralizing activin antibodies, or soluble activin receptor
579 antagonists (56), which allow concomitant suppression of both mDia2 and MIRO1 activities,
580 could be exploited to prevent the fibroblast-to-CAF reprogramming during tumor progression
581 and may also reduce the pro-tumorigenic activities of already existing CAFs. Suppression of
582 mitochondrial activity, *e.g.*, through cancer drugs that target mitochondrial metabolism in the
583 tumor cells, is a promising approach for cancer treatment (57). Our results strongly suggest that
584 perturbing mitochondrial positioning and function in CAFs may be therapeutically equally
585 important. Therefore, we advocate further exploration of the potential of activin antagonists, the

586 rational design of mDia2-specific formin inhibitors, and the development of next-generation
587 MIRO1 inhibitors for cancer treatment.

588 **Acknowledgments**

589 We thank Drs. Pino Bordignon and Gian-Paolo Dotto, University of Lausanne, for help with the
590 ear tumorigenesis assays, Dr. Petra Boukamp, Leibniz Institute for Environmental Medicine,
591 Düsseldorf, for SCC13 and HaCaT cells, Dr. Irini Vgenopoulou, ETH Zurich, for valuable
592 information on Seahorse analysis, and Drs. Jürg Hafner and Gaetana Restivo, University of
593 Zurich, for SCC biopsies or help with CAF isolation.

594

595 **Funding**

596 This work was supported by grants from Cancer Research Switzerland (KFS-4510-08-2018 to
597 S.W.), the Swiss National Science Foundation (grants 31003A_169204 and 31003B-189364 to
598 S.W), the Wilhelm-Sander Foundation (grants 2014-059.3 to S.W. and 2019-075.1 to Hans-
599 Dietmar Beer for the position of M.D.F.), University Medicine Zurich (Project SKINTEGRITY
600 to S.W.) and the ETH Zurich (Open ETH Project SKINTEGRITY.CH and core funding to S.W.
601 and M.K).

602

603 **Author contributions**

604 M.C. and S.W. designed the study; M.C., H.L., J.W., M.Z., and M.M. performed experiments
605 and analyzed data; M.D.F isolated the human CAFs; M.K provided reagents and expertise for
606 LEGENDPlex and Seahorse analyses; M.I. contributed to the design of the mDia2 and MIRO1
607 experiments and provided mDia2 expertise and reagents. M.C. wrote and S.W., M.I. edited the

608 manuscript, S.W. acquired the funding. All co-authors made important comments on the
609 manuscript.

610 **Figure legends**

611

612 **Fig. 1. mDia2 promotes protein secretion from HDFs**

613 A Quantification of total proteins secreted by sh-EV and -mDia2 HDFs. *n*=3.

614 B Representative Western blots of conditioned media (CM) of sh-EV and -mDia2
615 fibroblasts for fibronectin 1 (FN1), collagen (COL)4A1, and INHBA under reducing
616 conditions. Ponceau S staining of the membrane served as loading control.

617 C, D Representative immunofluorescence images of sh-EV and sh-mDia2 fibroblasts stained
618 for INHBA, FN1, and ELN (C), and quantification of intracellular fluorescence intensity
619 (D). *n*=3.

620 E Western blot for FN1, COL4, elastin (ELN) and vinculin (VIN, loading control) using
621 total lysates of sh-EV or -mDia2 fibroblasts. *n*=3.

622 F Representative FN1, COL1A1 and ELN immunofluorescence images and quantification
623 of the stained area in de-cellularized matrix from sh-EV and sh-mDia2 fibroblasts
624 cultured in glucose-containing medium. *n*=3.

625 G Interferon (IFN)- α 2, interleukin (IL)-1 β , and IL-6 concentrations (ng/ml) in
626 supernatants from sh-EV and -mDia2 fibroblasts. *n*=3.

627 H Quantification of SCC13 tumor spheroid area in hanging drop including CM from sh-
628 mDia2 and sh-EV fibroblasts and representative images (left). The area of the
629 spheroid formed in one control sample was set to 1. *n*=10-11.

630 I Western blots of total lysate from sh-EV or -mDia2 fibroblasts transfected with
631 expression vectors encoding wild-type mDia2 (WT), an actin-polymerization-deficient
632 mDia2 mutant (IA) or empty vector (pMX) for mDia2 and GAPDH.

633 J, K Percentage of total cells with actin stress fibers (J) and scratch closure (K) of sh-EV and
634 sh-mDia2 fibroblasts transfected with expression vectors encoding WT or IA mDia2 or
635 pMX. $n=3$ (J) and 6 (K).

636 L, M sh-EV or -mDia2 fibroblasts were transfected with expression vectors encoding WT or
637 IA mDia2 or pMX. Quantification of FN1 immunofluorescence staining of de-
638 cellularized ECM (L), and representative Western blot of total cell lysate and data
639 quantification (M). $n=3$.

640 Graphs show mean \pm SEM. ns $p>0.05$, $*p<0.05$, $**p<0.01$, $***p<0.001$, $****p<0.0001$ (one
641 way ANOVA with Bonferroni post-hoc test (D, E, J, K-M), or unpaired Student's t-test
642 (A, F-H)). Scale bars: 50 μm (C), 100 μm (F).

643

644 **Fig. 2. mDia2 regulates mitochondrial function in HDFs**

645 A Representative images of sh-EV and sh-mDia2 HDFs stained with MitoTracker (green),
646 rhodamine-coupled phalloidin (red) and Hoechst (blue). Graph shows fluorescence
647 intensity of MitoTracker relative to the highest intensity value. The relative distance is
648 indicated with values from 1 to 10 (see example on the top). $n=10$.

649 B Representative Western blots for mDia2, MIRO1 and HSP60 using cytoplasmic (Ct) and
650 mitochondrial (Mt) fractions, and total lysate (TL) of HDFs.

651 C, D sh-mDia2 fibroblasts were transfected with pMX-WT or pMX-IA expression vectors or
652 pMX, and stained with MitoTracker (C). sh-EV fibroblasts were used for comparison.

653 Bar graph shows fluorescence intensity distribution of MitoTracker relative to the highest
654 intensity value from the perinuclear region to the plasma membrane (D) as described in
655 (A). $n=6$.

656 E-G Representative images of sh-EV and sh-mDia2 HDFs stained with CellROX (E) or
657 MitoSOX (F) (red), counterstained with Hoechst (blue). Bar graphs show quantification
658 of staining intensity. Cells were analyzed for LDH release (G). $n=3-4$.

659 H Relative intracellular ATP levels in sh-EV or sh-mDia2 HDFs transfected with pMX-
660 WT, pMX-IA or pMX. $n=3$.

661 I Relative levels of mtDNA in sh-EV and sh-mDia2 HDFs determined by qPCR. $n=3$.

662 J Western blot of total lysate of sh-EV or -mDia2 fibroblasts for HSP60 and GAPDH, and
663 quantification of the HSP60/GAPDH ratio. $n=3$.

664 K Quantification of FN1- and COL I-stained area in de-cellularized matrix from sh-EV and
665 -mDia2 fibroblasts cultured in galactose-containing medium. $n=3$.

666 L Quantification of data from Seahorse analysis from sh-EV and sh-mDia2 HDFs cultured
667 in galactose-containing medium. $n=6$.

668 Graphs show mean \pm SEM. ns $p>0.05$, $*p<0.05$, $**p<0.01$, $***p<0.001$, $****p<0.0001$ (one-
669 way ANOVA with Bonferroni post-hoc test (H), two-way ANOVA with Bonferroni post-hoc
670 test (A, D), or unpaired Student's t-test (E-G, I-L)). Scale bars: 25 μm (A, C), 100 μm (E, F).

671

672 **Fig. 3. mDia2 binds and stabilizes MIRO1 in primary human fibroblasts**

673 A Representative Western blot of total lysate of sh-EV or -mDia2 fibroblasts for mDia2,
674 MIRO1, GAPDH, and α -tubulin.

675 B qRT-PCR analysis for *MIRO1* using RNA from sh-EV and sh-mDia2 HDFs. $n=3$.

676 C Representative Western blot of mitochondrial fractions from sh-EV and sh-mDia2
677 fibroblasts probed for mDia2, MIRO1 and HSP60, and quantification of mitochondrial
678 mDia2/HSP60 or MIRO1/HSP60 ratios. $n=3$.

679 D Representative images of sh-EV and sh-mDia2 HDFs immunostained for MIRO1 (red),
680 counterstained with MitoTracker (green) and Hoechst (blue). Dotted lines outline the cell
681 border.

682 E Western blot of total lysate from sh-EV or -mDia2 fibroblasts transfected with pMX-WT,
683 pMX-IA or pMX-control for MIRO1 and GAPDH, and quantification of the
684 MIRO1/GAPDH ratio. $n=3$.

685 F Representative Western blots for MIRO1 and vinculin using total lysates of sh-EV and
686 sh-mDia2 fibroblasts treated for 2 h with epoxomicin (EpoX) (10 μ M), and quantification
687 of the MIRO1/VINCULIN ratio. $n=3$ biological replicates.

688 G Representative images of sh-mDia2 fibroblasts treated with EpoX (10 μ M) or vehicle and
689 stained with MitoTracker (green) and rhodamine-coupled phalloidin (red). Bar graphs
690 show fluorescence intensity distribution of MitoTracker relative to the highest intensity
691 value from the perinuclear region to the plasma membrane and mean network branch
692 quantified using MiNA toolset. $n=22-29$.

693 H, I Representative images showing PLA signals (red) in HDFs stained with mDia2 and
694 MIRO1 antibodies and in the negative control (-Ctrl) without primary antibodies (H),
695 counterstained with Hoechst (blue), either alone (H) or together with MitoTracker (green)
696 (I).

697 Graphs show mean \pm SEM. ns $p>0.05$, * $p<0.05$, ** $p<0.01$, *** $p<0.001$, **** $p<0.0001$ (one-
698 way ANOVA with Bonferroni post-hoc test (E-G for network analysis), two-way ANOVA with
699 Bonferroni post-hoc test (G for MitoTracker intensity), or unpaired Student's t-test (B, C)). Scale
700 bars: 50 μ m.
701

702 **Fig. 4. Overexpression of *mDia2* and *MIRO1* in CAFs promotes tumorigenesis**

- 703 A Expression of *MIRO1* in liver, breast and ovarian cancer stroma (CS) vs. stroma of
704 respective normal tissues (NS) based on datasets GSE45001 (N=10 per group), GSE9014
705 (N=6 and 53), and GSE40595 (N=8 and 36).
- 706 B Single-cell expression profiles of *mDia2/DIAPH3* and *MIRO1* in immune cells,
707 endothelial cells and CAFs of melanomas based on data from Single Cell Portal (Broad
708 Institute).
- 709 C Correlation analysis between *MIRO1* and *mDia2*, *INHBA* and *TGFB1* gene expression
710 across different cancers using TIMER2. UVM: uveal melanoma; LUAD: lung
711 adenocarcinoma; PAAD: pancreatic ductal adenocarcinoma; SKCM: skin cancer
712 cutaneous melanoma, BRCA-Lum: luminal breast cancer; LIHC: liver hepatocellular
713 carcinoma. The red or blue color indicates a statistically significant positive/negative
714 correlation (Spearman's, $p < 0.05$), respectively, and gray denotes a non-significant
715 result.
- 716 D Kaplan–Meier survival curves based on TCGA and GTEx data. High expression of
717 *mDia2/DIAPH3* and *MIRO1* in patients with liver or lung cancer correlates with poor
718 survival.
- 719 E Representative sections from normal human skin, cSCC, and BCC stained for *MIRO1*.
720 Scale bars: 100 μ m. T: tumor cells.
- 721 F qRT-PCR analysis for *MIRO1* using RNA from CAFs or NFs from two SCC patients.
722 $n=3$.
- 723 G Representative Western blot of total lysates of NFs and CAFs from patient No. 1 for
724 *MIRO1*, CAF markers, and GAPDH.

- 725 H Quantification of SCC13 tumor spheroid area in hanging drop including CM from NF
726 and CAFs. *n*=10-11.
- 727 I Mitochondrial distribution in NFs or CAFs from patient No.1. *n*=15-19.
- 728 J Representative images and bar graph showing fluorescence intensity distribution of ATP
729 biosensor (cyto-Ruby3-iATPSnFR^{1.0}) relative to the highest intensity value from the
730 perinuclear region to the plasma membrane of NFs and CAFs (patient No. 1). *n*=19.
- 731 K Mitochondrial branch length of NFs or CAFs (patient No.1). *n*=15-19.
- 732 L Representative immunofluorescence images of de-cellularized matrices obtained from
733 NFs and CAFs (patient No.1) stained for FN1 and COL1A1 and quantification of stained
734 area. *n*=3.
- 735 M Quantification of SCC13 tumor spheroid area in hanging drop including CM from NFs
736 transfected with an expression vector encoding human MIRO1 (pGEM-MIRO1 “+”) or
737 empty vector (pGEM-EV “-”). The spheroid area in one control sample was set to 1.
738 *n*=10-12.
- 739 N SCC13 cells plated on either de-cellularized matrix from NFs transfected with pGEM-
740 MIRO1 or pGEM-EV. After 3 days, the number of Ki67-positive SCC13 cells was
741 quantified. *n*=3.
- 742 O Representative FN1 and COL1A1 immunofluorescence stainings and quantification of
743 stained area in de-cellularized matrix derived from NFs transfected with pGEM-MIRO1
744 or pGEM-EV. *n*=3.
- 745 P, Q sh-EV and sh-mDia2 fibroblasts were transfected with pGEM-MIRO1 (“+”) or pGEM-
746 EV (“-”). Expression of MIRO1 was analyzed by immunofluorescence 24 h post-
747 transfection (P). *n*=3. Bar graph shows fluorescence intensity distribution of MitoTracker

748 relative to the highest intensity value from the perinuclear region to the plasma
749 membrane (Q). $n=6-8$.
750 Bar graphs show mean \pm SEM. ns $p>0.05$, * $p<0.05$, ** $p<0.01$, *** $p<0.001$, **** $p<0.0001$ (one-
751 way ANOVA with Bonferroni post-hoc test (P), two-way ANOVA with Bonferroni post-hoc test
752 (I, J, Q), unpaired Student's t-test (A, F, H, K-O)). Scale bars: 50 μ m.

753

754 **Fig. 5. *MIRO1* is a target of activin A-SMAD2/3 signaling**

755 A HDFs were treated with 20 ng/ml activin A or vehicle for 6 h and analyzed for *MIRO1*
756 expression by qRT-PCR. $n=3$.
757 B ChIP using lysates from activin A- or vehicle-treated fibroblasts and a SMAD2/3
758 antibody, and amplification of the bound DNA with *MIRO1* primers (top). Pre-immune
759 serum (IgG) was used as negative control. Alignment of the sequences within the 2-kb
760 region upstream of the *MIRO1* gene transcription start site (TSS) of different species that
761 harbor a SMAD2/3 binding element (SBE) (in red and italics, bottom).
762 C, D Representative images of sections from ear skin tumors formed by SCC13 cells with
763 doxycycline (DOX)-inducible lentiviral overexpression of INHBA (SCC13 Act, (C)) or
764 FST – (SCC13 FST, (D)) or transduced with EV, immunostained for *MIRO1* (green) or
765 α -SMA (red), and counterstained with Hoechst (blue). Graphs show percentage of
766 *MIRO1*- relative to α -SMA-positive area (percentage of *MIRO1*⁺ area in stroma). $n=3$
767 tumors per group. Tumors were collected 5 or 12 weeks after the initial injection of
768 SCC13 Act or -FST. This accounts for the higher *MIRO1*-positivity of EV in (D)
769 compared to (C).

770 E Tumors formed by SCC13 Act cells were treated *ex vivo* for 6 h with 50 ng/ml follistatin,
771 immunostained for MIRO1 (green) or α -SMA (red), and counterstained with Hoechst
772 (blue). Graph shows percentage of MIRO1- relative to α -SMA-positive area. $n=4$.

773 F, G qRT-PCR for *FST* (F) and *MIRO1* (G) using RNA collected 24 h after DOX treatment
774 from clonally expanded HDFs transduced with empty vector (Fb EV) or with DOX-
775 inducible expression of FST (Fb FST1: clone 1, Fb FST2: clone 2). $n=3$.

776 H Western blots for MIRO1 and GAPDH using total lysates of Fb FST (clone 1) and Fb
777 EV.

778 I qRT-PCR for *DIAPH3* using RNA collected 24 h after DOX treatment from HDFs
779 transduced with Fb EV or Fb FST1. $n=3$.

780 J Representative images of Fb-EV or -FST1 stained with MitoTracker (green) and
781 Hoechst (blue).

782 K, L Fb FST1 and control fibroblasts were transfected with pGEM-MIRO1 (“+”) or pGEM-
783 EV (“-”). Expression of MIRO1 was analyzed by immunofluorescence 24 h post-
784 transfection (K). $n=3$. Graph shows fluorescence intensity distribution of MitoTracker
785 relative to the highest intensity value from the perinuclear region to the plasma
786 membrane (L). $n=8$.

787 M Quantification of SCC13 spheroid area in hanging drops including CM from Fb FST1
788 and their controls transfected with pGEM-MIRO1 or pGEM-EV. The area of the
789 spheroid in one control sample was set to 1. $n=8$.

790 Bar graphs show mean \pm SEM. ns $p>0.05$, * $p<0.05$, ** $p<0.01$, *** $p<0.001$ (one-way ANOVA
791 with Bonferroni post-hoc test (F, G, K, M), two-way ANOVA with Bonferroni post-hoc test (L),
792 or unpaired Student’s t-test (A, C-E, I)). Scale bars: 50 μ m (C-E), 25 μ m (J).

793

794 **Fig. 6. Knock-down of MIRO1 causes metabolic dysfunction and impaired protein**
795 **secretion in primary human skin CAFs**

796 A, B CAFs from patient No. 1 were transfected with MIRO1 (si-MIRO1) or control (si-Ctrl)
797 siRNAs. The knock-down was confirmed by qRT-PCR (A) and immunofluorescence
798 staining (B).

799 C Quantification of nuclear p53 in CAFs transfected with Ctrl or MIRO1 siRNAs. $n=3$.

800 D qRT-PCR for CAF marker genes and genes encoding different small GTPases using
801 RNA from si-MIRO1 or si-Ctrl CAFs. $n=3$.

802 E Representative images of si-MIRO1 or si-Ctrl CAFs (patient No.1) stained for MIRO1
803 (red), counterstained with MitoTracker (green) and Hoechst (blue).

804 F Quantification of COL1-stained area in de-cellularized matrix from si-Ctrl or si-MIRO1
805 CAFs. $n=3$.

806 G Relative levels of mitochondrial superoxide based on MitoSOX fluorescence intensity in
807 CAFs (patient No.1) transfected with si-Ctrl or si-MIRO1. $n=3$.

808 H CAFs (patient No.1) transfected with si-Ctrl or si-MIRO1 were analyzed for LDH
809 release. $n=3$.

810 I Seahorse assay for the OCR in CAFs (patient No.1) transfected with si-Ctrl or si-MIRO1
811 and quantification of basal respiration, maximal respiratory capacity, and ATP production
812 in glucose (top) or galactose (bottom) medium. $n=5-6$.

813 J Quantification of total proteins secreted by si-MIRO1 or si-Ctrl CAFs (patient No. 1) in
814 glucose medium. $n=6$.

815 K, L Representative images of immunofluorescence stainings for FN1 and COL1A (I) and
816 quantification of the stained area in de-cellularized matrix (J) from si-Ctrl or si-MIRO1
817 CAFs (patient No. 1) in glucose medium. $n=3$.
818 M Quantification of intracellular fluorescence in si-Ctrl or si-MIRO1 CAFs (patient No. 1)
819 immunostained for INHBA or ACTA2. $n=3$.
820 Bar graphs show mean \pm SEM. ns $p>0.05$, * $p<0.05$, ** $p<0.01$ (two-way ANOVA with
821 Bonferroni post-hoc test (D), unpaired Student's t-test (other graphs)). Scale bars: 50 μm (E) and
822 100 μm (B, K). Data shown in **Fig. 6K, L** were reproduced with CAFs from a second patient.
823

824 **Fig. 7. Depletion of MIRO1 in CAFs suppresses skin tumorigenesis**

825 A, B sh-EV or -mDia2 HDFs co-cultured for 7 days with SCC13 cells immunostained for E-
826 cadherin (red) and counterstained with MitoTracker (green) and Hoechst (blue) (A). The
827 mitochondrial distribution relative to the highest intensity value from the perinuclear
828 region of fibroblasts to the interface with SCC13 cells was quantified (B). Relative
829 distances range from 1-10. $n=4-6$.
830 C Representative Western blots for MIRO1, mDia2, and GAPDH using total lysates of NFs
831 and CAFs (patient No. 1) cultured with SMIFH2 (25 μM) or vehicle. The dotted line
832 indicates cutting of the membrane; all samples were loaded on the same gel.
833 D Representative images of NFs and CAFs cultured with SMIFH2 (25 μM) or vehicle and
834 stained with rhodamine-coupled phalloidin (red), MitoTracker (green) and Hoechst
835 (blue).
836 E Two-dimensional co-cultures of SCC13 cells with si-Ctrl or si-MIRO1 CAFs at day 7.
837 SCC13 cells were identified by E-cadherin (red) staining and counterstained with

838 MitoTracker (green) and Hoechst (blue). The mitochondrial distribution relative to the
839 highest intensity value from the perinuclear region of fibroblasts to the interface with
840 SCC13 cells was quantified. Relative distances range from 1-10. $n=12-14$.

841 F Chemotactic transwell migration of SCC13 cells using CM from si-Ctrl or si-MIRO1
842 CAFs. $n=3$.

843 G Quantification of SCC13 spheroid area in single hanging drop including CM from si-Ctrl
844 or si-MIRO1 CAFs. The spheroid area in one si-Ctrl sample was set to 1. $n=6$.

845 H Tumor volume at different time points 2 weeks after injection ($n=4$) and representative
846 photos of 2-week-old tumors formed upon intradermal co-injection of SCC13 cells with
847 si-MIRO1 or si-Ctrl CAFs. An inset panel indicates the area where tumor cells invade
848 into the cartilage. Asterisk indicates cartilage; arrow indicates site of invasion.

849 I Representative images of COL1A1 immunofluorescence and Herovici staining of tumors
850 formed by SCC13 cells transfected with si-MIRO1 or si-Ctrl CAFs at day 15.

851 J Quantification of percentage of COL1A1-positive area and curvature of fibers per field of
852 view. $n=3-4$.

853 K Increase in SCC13 (co-injected with CAFs) tumor volume (mm^3) upon injection of the
854 tumors with MIRO1-Reducer ($2.5 \mu\text{M}$ per injection) or vehicle (DMSO) once every 3-4
855 days for 18 days. Red arrows indicate the treatment time points. $n=5$.

856 Bar graphs show mean \pm SEM. ns $p>0.05$, * $p<0.05$, ** $p<0.01$, *** $p<0.001$, **** $p<0.0001$ (two-
857 way ANOVA with Bonferroni post-hoc test (B, E, H, K), unpaired Student's t-test (F, G, J)).
858 Scale bars: $25 \mu\text{m}$ (A, D, E) and $50 \mu\text{m}$ (I).

859 **References**

860

- 861 1. Sanz-Moreno V, Gaggioli C, Yeo M, Albregues J, Wallberg F, Viros A, *et al.* ROCK
862 and JAK1 signaling cooperate to control actomyosin contractility in tumor cells and
863 stroma. *Cancer Cell* **2011**;20:229-45
- 864 2. Baghban R, Roshangar L, Jahanban-Esfahlan R, Seidi K, Ebrahimi-Kalan A, Jaymand M,
865 *et al.* Tumor microenvironment complexity and therapeutic implications at a glance. *Cell*
866 *Commun Signal* **2020**;18:59
- 867 3. Sahai E, Astsaturov I, Cukierman E, DeNardo DG, Egeblad M, Evans RM, *et al.* A
868 framework for advancing our understanding of cancer-associated fibroblasts. *Nat Rev*
869 *Cancer* **2020**;20:174-86
- 870 4. Melchionna R, Spada S, Di Modugno F, D'Andrea D, Di Carlo A, Panetta M, *et al.* The
871 actin modulator hMENA regulates GAS6-AXL axis and pro-tumor cancer/stromal cell
872 cooperation. *EMBO Rep* **2020**;21:e50078
- 873 5. Innocenti M. New insights into the formation and the function of lamellipodia and ruffles
874 in mesenchymal cell migration. *Cell Adh Migr* **2018**;12:401-16
- 875 6. Isogai T, Innocenti M. New nuclear and perinuclear functions of formins. *Biochem Soc*
876 *Trans* **2016**;44:1701-8
- 877 7. Cangkrama M, Wietecha M, Mathis N, Okumura R, Ferrarese L, Al-Nuaimi D, *et al.* A
878 paracrine activin A-mDia2 axis promotes squamous carcinogenesis via fibroblast
879 reprogramming. *EMBO Mol Med* **2020**;12:e11466
- 880 8. Nishida Y, Nagatsuma AK, Kojima M, Gotohda N, Ochiai A. Novel stromal biomarker
881 screening in pancreatic cancer patients using the in vitro cancer-stromal interaction
882 model. *BMC Gastroenterol* **2020**;20:411
- 883 9. Cangkrama M, Wietecha M, Werner S. Wound Repair, Scar Formation, and Cancer:
884 Converging on Activin. *Trends Mol Med* **2020**;26:1107-17
- 885 10. Wietecha MS, Pensalfini M, Cangkrama M, Muller B, Jin J, Brinckmann J, *et al.* Activin-
886 mediated alterations of the fibroblast transcriptome and matrisome control the
887 biomechanical properties of skin wounds. *Nat Commun* **2020**;11:2604
- 888 11. Purdie KJ, Pourreyaon C, South AP. Isolation and culture of squamous cell carcinoma
889 lines. *Methods Mol Biol* **2011**;731:151-9

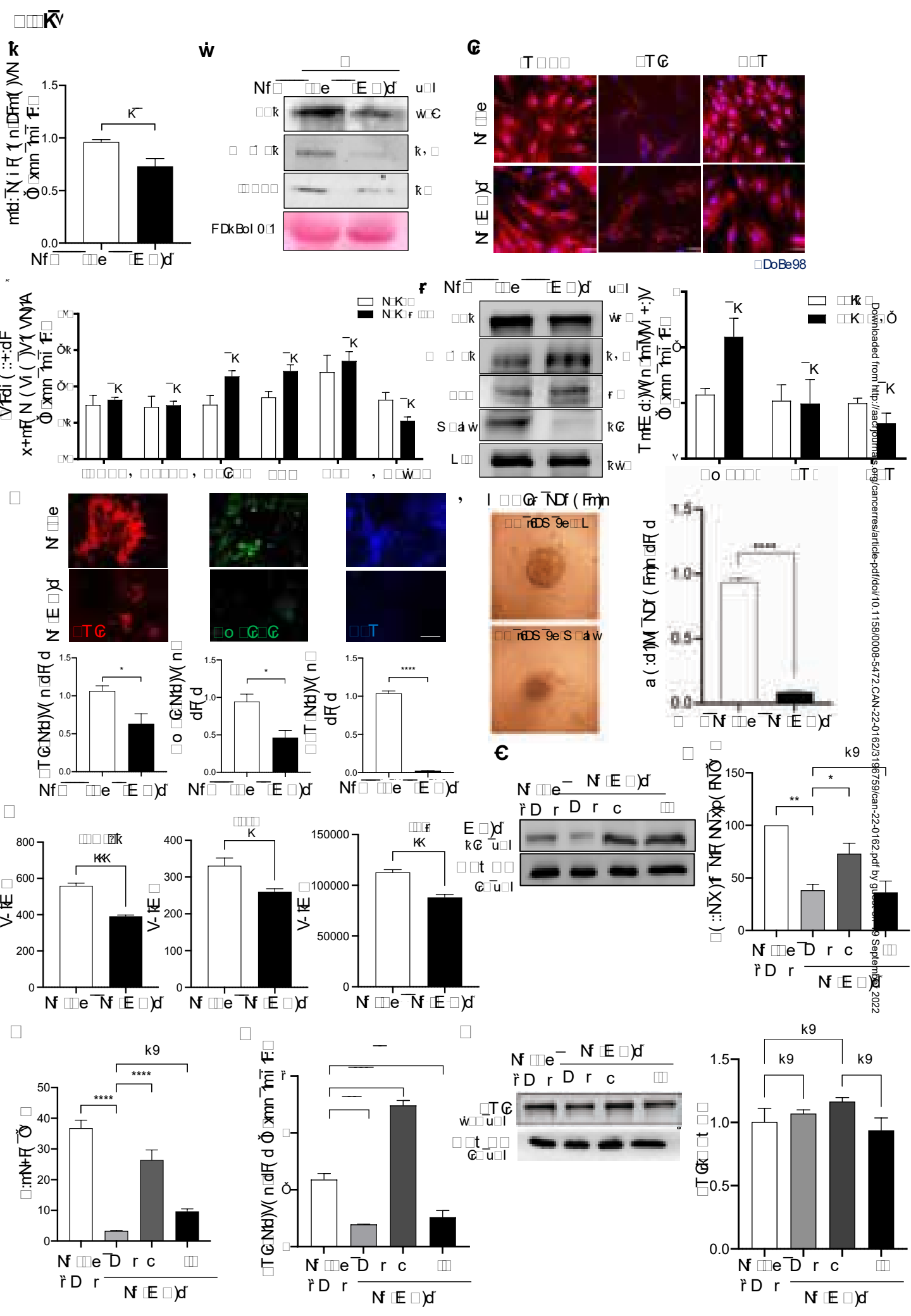
- 890 12. Procopio MG, Laszlo C, Al Labban D, Kim DE, Bordignon P, Jo SH, *et al.* Combined
891 CSL and p53 downregulation promotes cancer-associated fibroblast activation. *Nat Cell*
892 *Biol* **2015**;17:1193-204
- 893 13. Hiebert P, Wietcha MS, Cangkrama M, Haertel E, Mavrogonatou E, Stumpe M, *et al.*
894 Nrf2-Mediated Fibroblast Reprogramming Drives Cellular Senescence by Targeting the
895 Matrisome. *Dev Cell* **2018**;46:145-61 e10
- 896 14. Okumoto K, Ono T, Toyama R, Shimomura A, Nagata A, Fujiki Y. New splicing
897 variants of mitochondrial Rho GTPase-1 (Miro1) transport peroxisomes. *J Cell Biol*
898 **2018**;217:619-33
- 899 15. Li Q, Yao L, Wei Y, Geng S, He C, Jiang H. Role of RHOT1 on migration and
900 proliferation of pancreatic cancer. *Am J Cancer Res* **2015**;5:1460-70
- 901 16. Li W, Sancho A, Chung WL, Vinik Y, Groll J, Zick Y, *et al.* Differential cellular
902 responses to adhesive interactions with galectin-8- and fibronectin-coated substrates. *J*
903 *Cell Sci* **2021**;134
- 904 17. Isogai T, van der Kammen R, Goerdayal SS, Heck AJ, Altelaar AF, Innocenti M.
905 Proteomic analyses uncover a new function and mode of action for mouse homolog of
906 Diaphanous 2 (mDia2). *Mol Cell Proteomics* **2015**;14:1064-78
- 907 18. Isogai T, van der Kammen R, Innocenti M. SMIFH2 has effects on Formins and p53 that
908 perturb the cell cytoskeleton. *Sci Rep* **2015**;5:9802
- 909 19. Seltmann K, Meyer M, Sulcova J, Kockmann T, Wehkamp U, Weidinger S, *et al.*
910 Humidity-regulated CLCA2 protects the epidermis from hyperosmotic stress. *Sci Transl*
911 *Med* **2018**;10
- 912 20. Isogai T, van der Kammen R, Bleijerveld OB, Goerdayal SS, Argenzio E, Altelaar AF, *et*
913 *al.* Quantitative Proteomics Illuminates a Functional Interaction between mDia2 and the
914 Proteasome. *J Proteome Res* **2016**;15:4624-37
- 915 21. Lobas MA, Tao R, Nagai J, Kronschlager MT, Borden PM, Marvin JS, *et al.* A
916 genetically encoded single-wavelength sensor for imaging cytosolic and cell surface
917 ATP. *Nat Commun* **2019**;10:711
- 918 22. Schindelin J, Arganda-Carreras I, Frise E, Kaynig V, Longair M, Pietzsch T, *et al.* Fiji:
919 an open-source platform for biological-image analysis. *Nat Methods* **2012**;9:676-82

- 920 23. Wershof E, Park D, Barry DJ, Jenkins RP, Rullan A, Wilkins A, *et al.* A FIJI macro for
921 quantifying pattern in extracellular matrix. *Life Sci Alliance* **2021**;4
- 922 24. Valente AJ, Maddalena LA, Robb EL, Moradi F, Stuart JA. A simple ImageJ macro tool
923 for analyzing mitochondrial network morphology in mammalian cell culture. *Acta*
924 *Histochem* **2017**;119:315-26
- 925 25. Wilanowski T, Caddy J, Ting SB, Hislop NR, Cerruti L, Auden A, *et al.* Perturbed
926 desmosomal cadherin expression in grainy head-like 1-null mice. *EMBO J* **2008**;27:886-
927 97
- 928 26. Dowell JA, Johnson JA, Li L. Identification of astrocyte secreted proteins with a
929 combination of shotgun proteomics and bioinformatics. *J Proteome Res* **2009**;8:4135-43
- 930 27. Peirsman A, Blondeel E, Ahmed T, Anckaert J, Audenaert D, Boterberg T, *et al.*
931 MISpheroid: a knowledgebase and transparency tool for minimum information in
932 spheroid identity. *Nat Methods* **2021**;18:1294-303
- 933 28. Foty R. A simple hanging drop cell culture protocol for generation of 3D spheroids. *J Vis*
934 *Exp* **2011**
- 935 29. Barrett T, Wilhite SE, Ledoux P, Evangelista C, Kim IF, Tomashevsky M, *et al.* NCBI
936 GEO: archive for functional genomics data sets--update. *Nucleic Acids Res*
937 **2013**;41:D991-5
- 938 30. Tang Z, Kang B, Li C, Chen T, Zhang Z. GEPIA2: an enhanced web server for large-
939 scale expression profiling and interactive analysis. *Nucleic Acids Res* **2019**;47:W556-
940 W60
- 941 31. Li T, Fu J, Zeng Z, Cohen D, Li J, Chen Q, *et al.* TIMER2.0 for analysis of tumor-
942 infiltrating immune cells. *Nucleic Acids Res* **2020**;48:W509-W14
- 943 32. Goswami CP, Nakshatri H. PROGgene: gene expression based survival analysis web
944 application for multiple cancers. *J Clin Bioinforma* **2013**;3:22
- 945 33. Cox TR. The matrix in cancer. *Nat Rev Cancer* **2021**;21:217-38
- 946 34. Lodberg A. Principles of the activin receptor signaling pathway and its inhibition.
947 *Cytokine Growth Factor Rev* **2021**;60:1-17
- 948 35. Beli P, Mascheroni D, Xu D, Innocenti M. WAVE and Arp2/3 jointly inhibit filopodium
949 formation by entering into a complex with mDia2. *Nat Cell Biol* **2008**;10:849-57

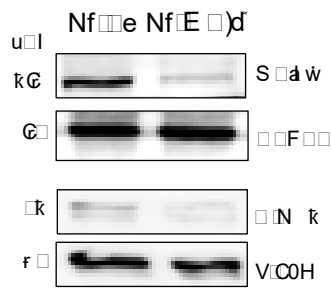
- 950 36. Martinez J, Marmisolle I, Tarallo D, Quijano C. Mitochondrial Bioenergetics and
951 Dynamics in Secretion Processes. *Front Endocrinol (Lausanne)* **2020**;11:319
- 952 37. Moore AS, Coscia SM, Simpson CL, Ortega FE, Wait EC, Heddleston JM, *et al.* Actin
953 cables and comet tails organize mitochondrial networks in mitosis. *Nature* **2021**;591:659-
954 64
- 955 38. Rossignol R, Gilkerson R, Aggeler R, Yamagata K, Remington SJ, Capaldi RA. Energy
956 substrate modulates mitochondrial structure and oxidative capacity in cancer cells.
957 *Cancer Res* **2004**;64:985-93
- 958 39. Lopez-Domenech G, Covill-Cooke C, Ivankovic D, Halff EF, Sheehan DF, Norkett R, *et*
959 *al.* Miro proteins coordinate microtubule- and actin-dependent mitochondrial transport
960 and distribution. *EMBO J* **2018**;37:321-36
- 961 40. Wang X, Winter D, Ashrafi G, Schlehe J, Wong YL, Selkoe D, *et al.* PINK1 and Parkin
962 target Miro for phosphorylation and degradation to arrest mitochondrial motility. *Cell*
963 **2011**;147:893-906
- 964 41. Tsherniak A, Vazquez F, Montgomery PG, Weir BA, Kryukov G, Cowley GS, *et al.*
965 Defining a Cancer Dependency Map. *Cell* **2017**;170:564-76 e16
- 966 42. Verstreken P, Ly CV, Venken KJ, Koh TW, Zhou Y, Bellen HJ. Synaptic mitochondria
967 are critical for mobilization of reserve pool vesicles at *Drosophila* neuromuscular
968 junctions. *Neuron* **2005**;47:365-78
- 969 43. Onodera Y, Nam JM, Horikawa M, Shirato H, Sabe H. Arf6-driven cell invasion is
970 intrinsically linked to TRAK1-mediated mitochondrial anterograde trafficking to avoid
971 oxidative catastrophe. *Nat Commun* **2018**;9:2682
- 972 44. Langert KA, Pervan CL, Stubbs EB, Jr. Novel role of Cdc42 and RalA GTPases in TNF-
973 alpha mediated secretion of CCL2. *Small GTPases* **2014**;5
- 974 45. Ding L, Lei Y, Han Y, Li Y, Ji X, Liu L. Vimar Is a Novel Regulator of Mitochondrial
975 Fission through Miro. *PLoS Genet* **2016**;12:e1006359
- 976 46. Schuler MH, Lewandowska A, Caprio GD, Skillern W, Upadhyayula S, Kirchhausen T,
977 *et al.* Miro1-mediated mitochondrial positioning shapes intracellular energy gradients
978 required for cell migration. *Mol Biol Cell* **2017**;28:2159-69

- 979 47. Liang Y, Lv Z, Huang G, Qin J, Li H, Nong F, *et al.* Prognostic significance of abnormal
980 matrix collagen remodeling in colorectal cancer based on histologic and bioinformatics
981 analysis. *Oncol Rep* **2020**;44:1671-85
- 982 48. Hsieh CH, Li L, Vanhauwaert R, Nguyen KT, Davis MD, Bu G, *et al.* Miro1 Marks
983 Parkinson's Disease Subset and Miro1 Reducer Rescues Neuron Loss in Parkinson's
984 Models. *Cell Metab* **2019**;30:1131-40 e7
- 985 49. Schworer S, Berisa M, Violante S, Qin W, Zhu J, Hendrickson RC, *et al.* Proline
986 biosynthesis is a vent for TGFbeta-induced mitochondrial redox stress. *EMBO J*
987 **2020**;39:e103334
- 988 50. Avagliano A, Granato G, Ruocco MR, Romano V, Belviso I, Carfora A, *et al.* Metabolic
989 Reprogramming of Cancer Associated Fibroblasts: The Slavery of Stromal Fibroblasts.
990 *Biomed Res Int* **2018**;2018:6075403
- 991 51. Kruppa AJ, Buss F. Actin cages isolate damaged mitochondria during mitophagy.
992 *Autophagy* **2018**;14:1644-5
- 993 52. Majstrowicz K, Honnert U, Nikolaus P, Schwarz V, Oeding SJ, Hemkemeyer SA, *et al.*
994 Coordination of mitochondrial and cellular dynamics by the actin-based motor Myo19. *J*
995 *Cell Sci* **2021**;134
- 996 53. Gao J, Sang M, Zhang X, Zheng T, Pan J, Dai M, *et al.* Miro1-mediated mitochondrial
997 dysfunction under high nutrient stress is linked to NOD-like receptor 3 (NLRP3)-
998 dependent inflammatory responses in rat pancreatic beta cells. *Free Radic Biol Med*
999 **2015**;89:322-32
- 1000 54. Stephen TL, Higgs NF, Sheehan DF, Al Awabdh S, Lopez-Domenech G, Arancibia-
1001 Carcamo IL, *et al.* Miro1 Regulates Activity-Driven Positioning of Mitochondria within
1002 Astrocytic Processes Apposed to Synapses to Regulate Intracellular Calcium Signaling. *J*
1003 *Neurosci* **2015**;35:15996-6011
- 1004 55. Villanueva J, Viniegra S, Gimenez-Molina Y, Garcia-Martinez V, Exposito-Romero G,
1005 del Mar Frances M, *et al.* The position of mitochondria and ER in relation to that of the
1006 secretory sites in chromaffin cells. *J Cell Sci* **2014**;127:5105-14
- 1007 56. Inman GJ, Nicolas FJ, Callahan JF, Harling JD, Gaster LM, Reith AD, *et al.* SB-431542
1008 is a potent and specific inhibitor of transforming growth factor-beta superfamily type I

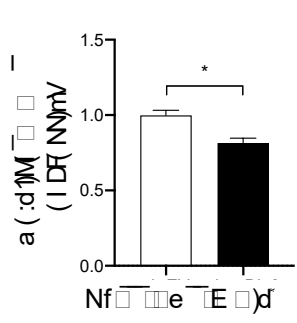
1009 activin receptor-like kinase (ALK) receptors ALK4, ALK5, and ALK7. *Mol Pharmacol*
1010 **2002**;62:65-74
1011 57. Porporato PE, Filigheddu N, Pedro JMB, Kroemer G, Galluzzi L. Mitochondrial
1012 metabolism and cancer. *Cell Res* **2018**;28:265-80
1013



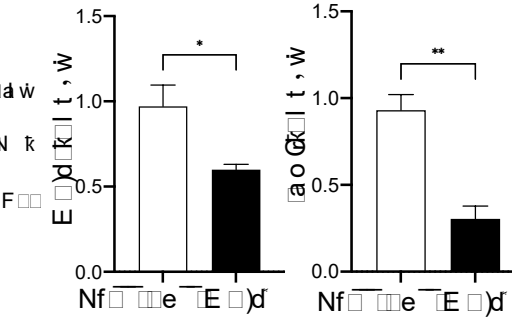
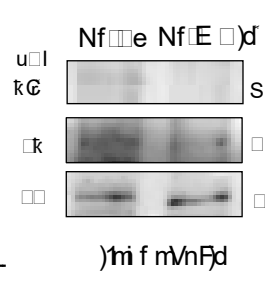
k



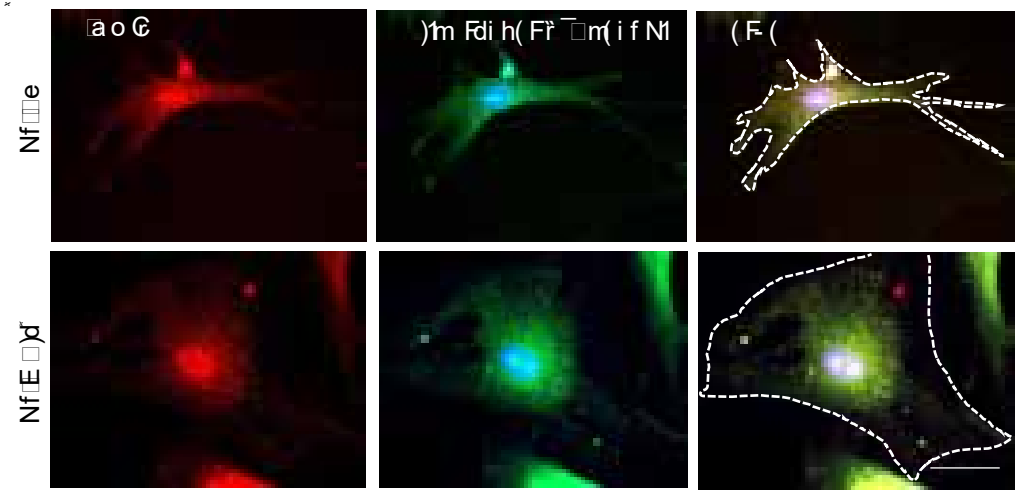
w



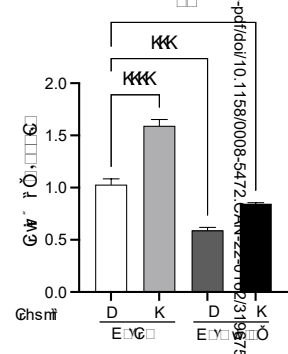
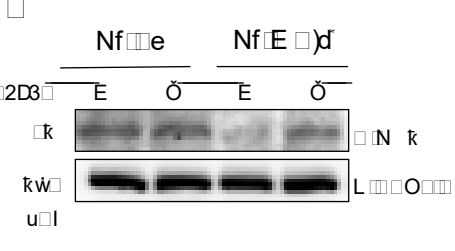
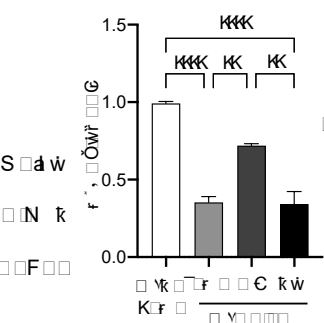
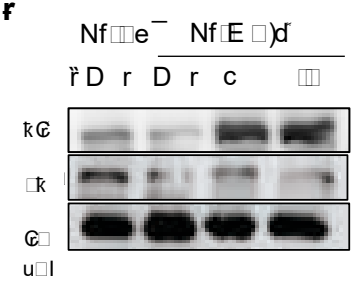
G



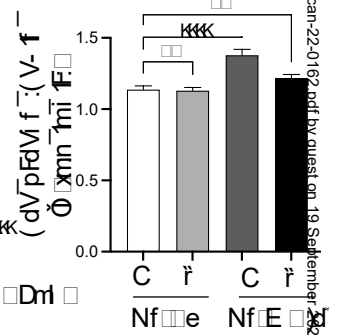
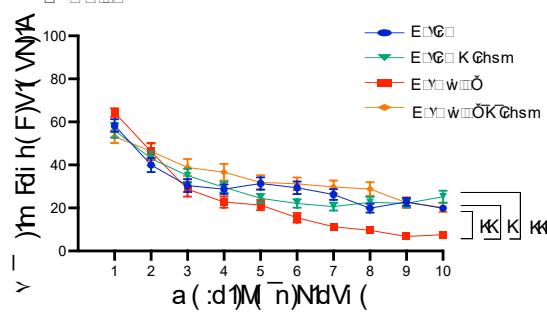
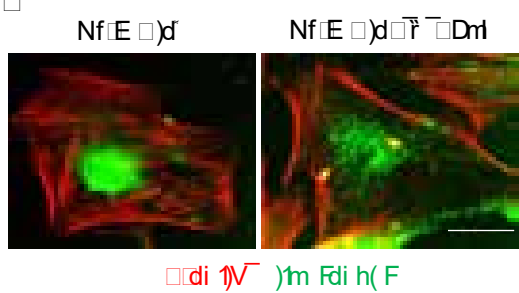
x



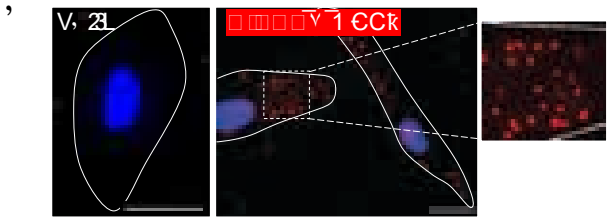
f



y



z



c

